NANO LETTERS

Communication

Very high surface area mesoporous thin films of SrTiO grown by pulsed laser deposition and application to efficient photoelectrochemical water splitting

Abhijeet Laxman Sangle, Simrjit Singh, Jie Jian, Sneha Rohita Bajpe, Haiyan Wang, Neeraj Khare, and Judith L. MacManus Driscoll

Nano Lett., **Just Accepted Manuscript** • DOI: 10.1021/acs.nanolett.6b02487 • Publication Date (Web): 24 Oct 2016

ACS Publications

Nano Letters is published by the American Chemical Society. 1155 Sixteenth Street N.W., Washington, DC 20036

Very high surface area mesoporous thin films of $SrTiO_3$ grown by pulsed laser deposition and application to efficient photoelectrochemical water splitting

Abhijeet Sangle[†,*], Simrjit Singh[§], Jie Jian[t], Sneha R. Bajpe[†], Haiyan Wang[t], Neeraj Khare[§] and Judith L. MacManus-Driscoll[†,*]

[†] Department of Materials Science and Metallurgy, University of Cambridge, Cambridge-CB3 0FS, United Kingdom

[§] Department of Physics, Indian Institute of Technology Delhi, New Delhi-110016, India

[t] Electrical and Computer Engineering 3128, Texas A & M University, College Station, Texas 77843, United States

[*]Corresponding authors: as2174@cam.ac.uk, jld35@cam.ac.uk

Abstract: Very high surface area, self-assembled, highly crystalline mesoporous $SrTiO_3$ (STO) thin films were developed for photoelectrochemical water splitting. Much improved performance of these mesoporous films compared to planar STO thin films and any other form of STO such as single crystal samples and nanostructures was demonstrated. The high performance resulted from very large surface area films and optimisation of carrier concentration.

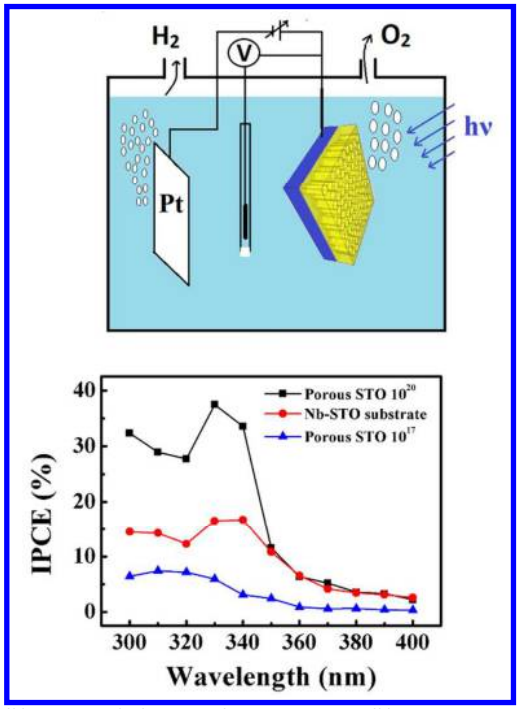

Keywords: Pulsed Laser Deposition, Self-assembled nanocomposite films, Mesoporous crystalline thin films, High surface area films, Photoelectrochemical water splitting, $SrTiO_3$

Since the discovery of photoelectrochemical water splitting using TiO_2 by Honda and Fujishima[1], this type of renewable energy generation has captured the attention of the researchers worldwide. There have been hundreds of different materials used by researchers for this purpose. They can be broadly classified as transition metal chalcogenides, III-V semiconductors, Group IV elemental and compound semiconductors, and transition metal oxides. Except for a few, most of the photocatalyst materials suffer from one or more drawbacks such as chemical instability[2–7], environmental toxicity[8] , unfavourable band positions[3–5], overpotential loss[9] or scarce availability leading to high costs[10]. Transition metal oxides are the most widely researched group of photocatalysts and oxides, for example, STO and $BaSnO_3$ have been shown to not be limited by the aforementioned drawbacks[11]. Wrighton *et al.*[12], in 1976, first demonstrated the usefulness of STO for light assisted water splitting, thus making it the first material discovered to be suitable for photocatalytic water splitting, without even applying any external bias[13]. Since then, STO has been shown to be an effective photoelectrochemical (PEC) water splitting material. While STO absorbs only a small portion of the visible light, impurity levels can be added in the bandgap to tune the bandgap so it is more suitable for visible absorption. The visible light absorption of STO can be improved by doping STO with metallic[14–16] and non-metallic impurities[17,18]. Moreover, the performance can be further enhanced by growing tandem PEC cells, where STO is coated with a suitable material with a bandgap in tandem to that of STO. The conduction band of STO is 200 meV more negative than the conduction band of TiO_2 (anatase), making it energetically more favourable for photo-assisted water splitting[19,20]. In addition, STO has excellent chemical and photochemical stability[13,21–23] and high quality STO is reported to have much higher electron mobility (5-8 cm^2V/s) compared to TiO_2 (0.1-4 cm^2V/s)[24]. While ZnO is a popular PEC water splitting material which has similar band positions to TiO_2 and is easy to grow in nanostructured form, it too is inferior to STO since it undergoes

photocorrosion when put in an aqueous solution under UV light; it even gets corroded in the dark when in an alkaline medium[25].

Many reports of using STO for photoelectrochemical water splitting are for materials made in either bulk[8,21] or nanopowder[26–30] form. While nanopowders have the obvious advantage over bulk form of higher surface area/volume ratio, thus increasing the number of reaction sites for water splitting, they cannot be easily recovered from the electrolyte[31–34] Moreover, usually the nanopowders are coated with co-catalysts like Pt[30,35,36], IrO_2[27] or Au[37], which act as cathodes for evolution of H_2. Not only are these co-catalysts expensive, but both H_2 and O_2 gases evolve in close proximity[23,34], which is undesirable. Also, the co-catalysts rob the photocatalysts of useful light-exposed surface[23]. Finally, nanopowder STO photocatalysts rely solely on photo-assisted water splitting without electric field assistance for the hydrogen evolution process[26].

Many of the above disadvantages of using either bulk or nanopowder photocatalysts can be eliminated if nanostructured photocatalysts are fixed to a conducting substrate, thus making them easier to be recovered and reused. Also, gas separation is easier, as the anode and cathode can be spatially separated. Some groups have coated nanopowders on conducting substrates to immobilise them[26]. However, the high surface area advantage offered by nanopowders is lost if the nanopowders are simply coated on a conducting substrate, as the specific surface area is substantially reduced. Moreover, because of the higher number of grain boundaries and poor particle-to-particle contact in coated nanopowders, recombination losses are higher.

A way to overcome the aforementioned problems of nanopowders is to use oriented, substrate anchored nanotubes/nanorods. Such structures allow for directional charge carrier transport offered without reduction of the surface area, as well as less recombination

losses[20,31,38–43]. There are some investigations of oriented chemically grown mesoporous films of $SrTiO_3$[20,44–46], but only one of those reports is for photoelectrochemical water splitting and the performance is well below that of TiO_2[20]. Improved performance is realised in hydrothermally grown heterojunctions of TiO_2 nanotubes coated with STO[20,47–49] (Table 1). Such heterojunctions give rise to cascading bandgaps, which leads to efficient charge separation and reduced recombination losses leading to significantly better performance than chemically grown plain STO films[22,50–53] (Table 1).

As far as known, there are no reports of physical vapour deposited (PVD) nanostructured or mesostrutured STO films for PEC water splitting. On the other hand, such films have strong potential for improved performance over chemically grown materials, owing to their high crystalline perfection. Moreover, since there are no chemical reactions taking place, there is lesser chance of by-product impurities from these reactions getting incorporated in the films[54]. Hence, lower defect concentrations are expected compared to chemically grown nanostructures[55]. Indeed, in chemically grown films, annealing at moderate temperatures does not appreciably reduce the defect density[56,57]. Another advantage of PVD grown films is that they are very well-anchored to the substrate allowing for reuse many times. Finally, as described in this work, use of new composite structures, allows for creation of very high surface area films.

The aim of this work is to explore the photoelectrochemical water splitting performance of PVD grown mesoporous thin films. Highly crystalline, well-oriented, epitaxial films of STO with appropriate treatment to strongly increase surface area are used for this study. We show much improved water splitting performance over previous reports on STO.

In brief, to create the mesoporous films, first columnar composite thin films of MgO and STO were grown on Nb-STO (001) substrates (10 x 5 x 0.5 mm^3 in size) using pulsed

laser deposition (PLD) (figure 1(a)). These films consist of epitaxial nanopillars (diameter ~20 nm) of MgO embedded in a matrix of STO (figure 1(b)). After fabrication of the composite films, the MgO phase was selectively etched out (figure 1(c)), leaving behind a high surface area honeycomb structure.

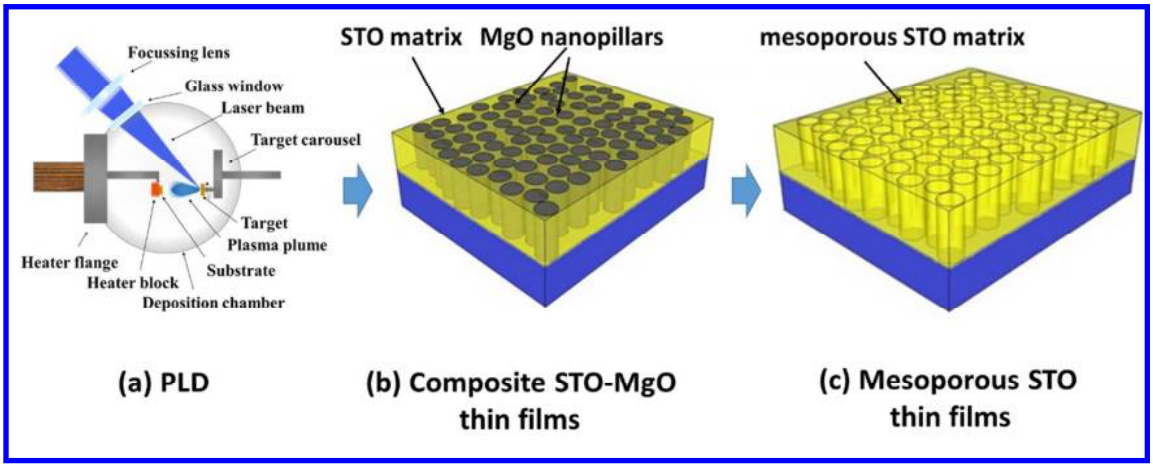

Figure 1: Schematic diagram showing (a) the PLD setup, (b) the PLD-grown columnar composite thin film containing STO matrix and MgO nanopillars and (c) the mesoporous STO thin film, after etching out the MgO nanopillars

Figure 2(a) is a plan-view SEM image of the composite thin film prior to etching, showing MgO nanopillars dispersed in the matrix of STO. The acidic etchant solution dissolves the alkaline MgO phase selectively, leaving the STO phase intact, as can be seen in Figure 2(b). Figure 2(c) shows an X-ray diffraction pattern of a composite film before and after etching the MgO nanopillars. From the 2θ-ω scans, it can be clearly seen that MgO grows with the same orientation as STO (001) single crystal. The STO film peaks overlap with the substrate peaks because of their very similar lattice parameter. We note, however, that the lattice parameters of the STO film and STO substrate are not necessarily identical owing to the vertical strain effects in the composite. The epitaxial quality of STO/MgO films grown on STO substrate is excellent, as we have shown in an earlier study[58]. The MgO peak which was

present before etching is found to have disappeared after etching (Figure 2(c)). A cross-sectional TEM view of a typical mesoporous STO film is shown in Figure 2(d).

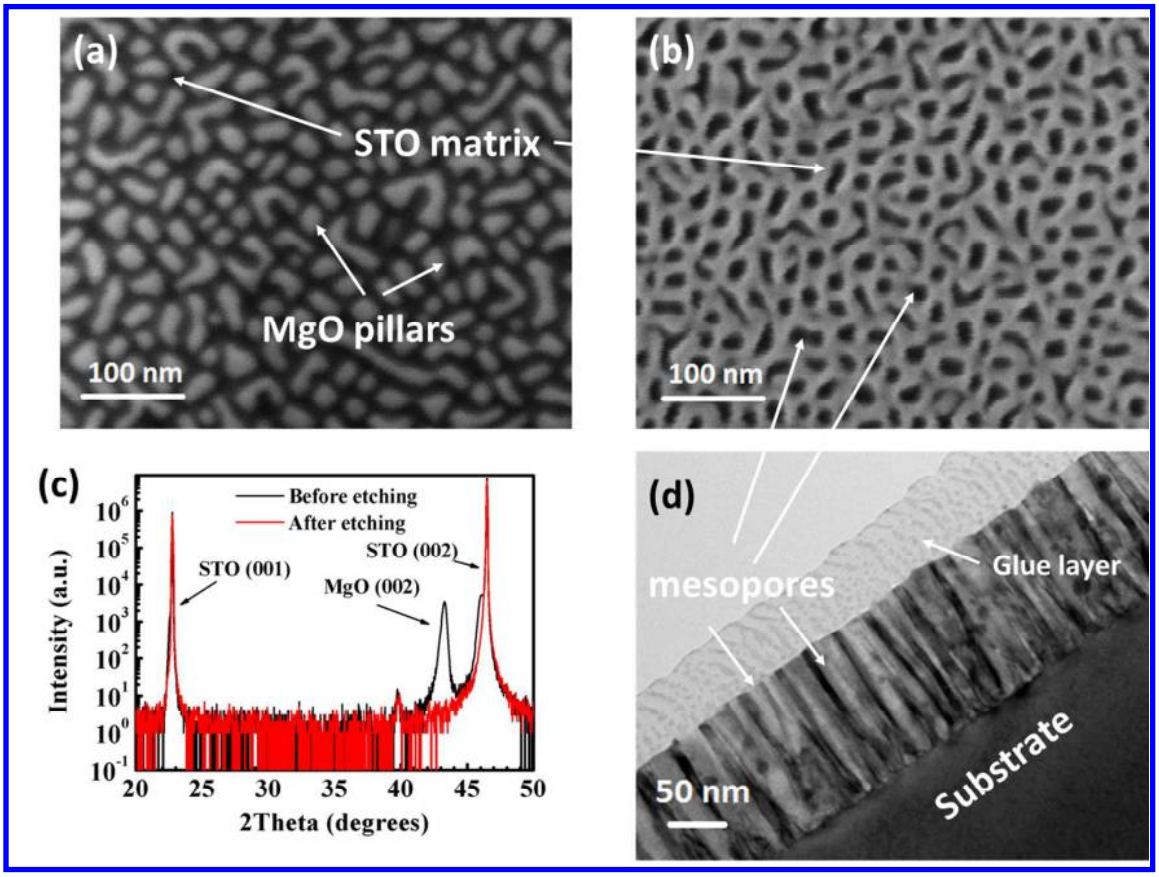

Figure 2: Plan-view SEM image of STO-MgO columnar composite thin film (a) before etching out the MgO nanopillars, and (b) after etching out the MgO nanopillars; (c) X-ray diffraction, out-of-plane 2θ-ω scans showing disappearing MgO peaks after etching, thus confirming the completion of the etching process, and (d) Cross-sectional TEM image of a typical porous STO thin film showing oriented mesopores (diameter ~20 nm). (As shown in the figure, the top layer is the glue layer used to glue the two pieces together before sample preparation).

From Figure 2(d), we can see that the mesopores are highly oriented in a direction perpendicular to the substrate surface. The SEM image (Figure 2(a)) shows that the mesopores are of diameter ~20 nm, and the wall-thickness of the surrounding STO is 5-7 nm.

This roughly translates to a 2500% increase in surface area over the surface of the substrate. Comparing with mesoporous STO films of same thickness made by the hydrothermal method[59], the mesoporous STO films of this study have ~ 5 times surface area.

The PLD grown films can be doped in a controlled manner[60] to achieve an optimum carrier concentration, which is important for photoelectrochemical water splitting. Stoichiometric STO has poor electrical conductivity and thus it is not suitable to act as a photoelectrode, since the excited charge carriers need to be extracted easily for good water splitting efficiency. The conductivity of STO can be increased by doping with donor impurities such as Nb^{5+} or self-doping with oxygen[22,61,62]. Oxygen vacancies are created by annealing the material in a reducing environment[33,61], in accordance with equation (1) -

$$SrTiO_3 \rightarrow Sr^{2+}{}_{Sr^{2+}} + Ti^{4+}{}_{Ti^{4+}} + (3-\delta)O^{2-}{}_{O^{2-}} + \delta\ddot{V}_{O^{2-}} + 2e^- + \frac{\delta}{2}O_{2(g)}\uparrow \quad (1)$$

The oxygen vacancies act as shallow donors[63] and each vacancy donates two electrons. This increases the charge carrier density in the semiconductor, and thus improves its conductivity.

Results

Three mesoporous samples of different carrier concentration were studied – (a) a Nb-STO substrate (as received), (b) a porous STO film post-annealed in high oxygen partial pressure (400 mbar O_2), termed Porous STO 10^{17}, and (c) a porous STO film post-annealed in low oxygen partial pressure (0.2 mbar O_2), termed Porous STO 10^{20}. The above labelling of the samples is based on their charge carrier concentrations (in number per cm^3), which we determine later.

The key photoelectrochemical water splitting results and the comparison of the samples of this work with literature data are shown in Table 1. The first thing to note in Table

1 is that the different annealing conditions have brought about a three orders of magnitude of difference in charge carrier density from 10^{17} - 10^{20} cm^{-3}. A carrier concentration of the order of ~10^{19}-10^{20} cm^{-3} is normally desired for effective water splitting performance[64–66]. Hence, we have produced samples in this optimised carrier concentration range.

Table 1: Results of the measurements for the different samples of this work compared to other STO samples in the literature. V_{fb} is the flat band potential measured vs. the Ag/AgCl (3M KCl) reference electrode, N_D is the charge carrier density obtained $1/C^2$ vs. V plots (as discussed later). The incident photon to current efficiency (IPCE) was obtained at 0.5 V vs. Ag/AgCl (3M KCl).

	Sample	V_{fb} (V) vs. V(Ag/AgCl) (3M KCl) (V)	N_D (cm^{-3})	Highest values of IPCE
1.	Porous STO 10^{17} (this work)	-0.75	1.38 x 10^{17}	12% at 330 nm and 0.3 V vs. Ag/AgCl (3M KCl) (~1.30 V vs RHE)
2.	Porous STO 10^{20} (this work)	-0.60	2.80 x 10^{20}	38% at 330 nm and 0.3 V vs. Ag/AgCl (3M KCl) (~1.30 V vs. RHE)
3.	Nb-STO substrate (this work)	-1.00	1.90 x 10^{19}	16% at 330 nm and 0.3 V vs. Ag/AgCl (3M KCl) (~1.30 V vs. RHE)
4.	Colloidal suspension dip-coated Nb-doped STO thin film	-0.79	1.50 x 10^{20}	26% at 290 nm and at 1.23 V vs. RHE[22]
5.	Hydrothermally grown STO films decorated with carbon quantum dots	--	--	14% at 340 nm and at 1.23 V vs. RHE[50]
6.	Ir doped STO single crystals	-0.1 V vs. Ag/AgCl (0.4 V vs. RHE) (onset potential)		4% at 400 nm at 1 V vs. Ag/AgCl[67] (~1.5 V vs. RHE)
7.	Hydrothermally grown STO-TiO_2 heterostructures	-0.980 vs. (SCE) (~0.03 V vs. RHE)		6.55% at 360 nm and no external bias[20]
		--	--	27% at 330 nm and no external bias[47]
		-0.84 V (vs. SCE) or (~ -0.19 vs. RHE)	--	50% at 355 nm at 0.6 V vs. SCE[48] (~1.25 V vs. RHE)

From Table 1, we can see that porous STO 10^{20} shows much improved IPCE values over the Nb-STO substrate and at 38% is one of the best efficiencies reported for plain STO in the literature. Also, it is comparable to some of the highest results reported for STO-TiO_2 heterostructures[47,48].

In Table 1, the flat band potential (V_{fb}) values are also compared for the different samples. V_{fb} is an important parameter for photoelectrochemical water splitting as it gives us a direct measure of band bending in the sample, and hence it can tell us about the onset potential. The V_{fb} for porous STO 10^{20} is higher (more positive) than that for porous STO 10^{17}. This can be explained by presence of surface states in porous STO 10^{20} which are absent or scarcely present in porous STO 10^{17}. The high oxygen vacancy concentration leads to high N_D. However, at the same time, generation of a high concentration of oxygen vacancies means that the number of surface states is also high. A more detailed discussion about V_{fb} and presence of surface states can be found in the supplementary information.

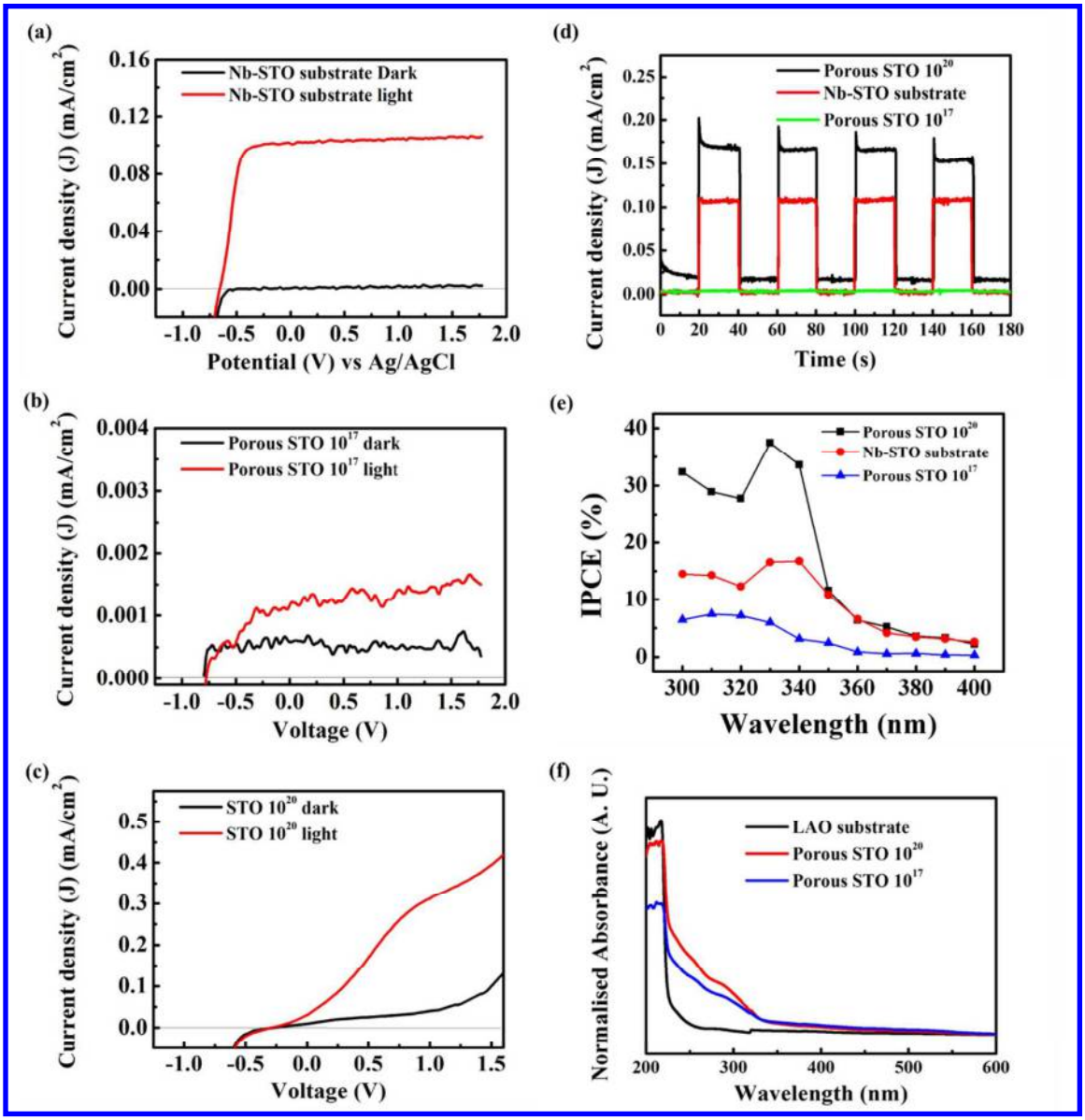

Figure 3: J-V characteristics of (a) Nb-STO substrate, (b) porous STO 10^{17} and (c) porous STO 10^{20}. (d) Chronoamperometry results of the samples. The potential used was 0.5 V vs. the Ag/AgCl (3M KCl) electrode for Chronoamperometry results. (e) Incident Photon to Current Efficiency (IPCE) results measured at 0.3 V vs. Ag/AgCl and (f) UV-Vis absorption spectra.

Now we look at the current density vs. applied potential (J-V) characteristics, comparing the photocurrent of all the three samples reported in this study. Figure 3 (a), (b)

and (c) show J-V characteristics of Nb-STO, porous STO 10^{17} and porous STO 10^{20}, respectively, in light and dark conditions. It can be clearly seen from Figure 3(a), (b) and (c) that porous STO 10^{20} shows much improved photocurrent over the flat Nb-STO substrate. This is consistent with the higher surface area and higher carrier concentration in porous STO 10^{20}. Also, as expected, the photocurrent is higher in porous STO 10^{20} than in porous STO 10^{17} on account of the better conductivity of porous STO 10^{20}. The current values are higher than those achieved for STO thin films previously reported [22,50].

It can be seen that porous STO 10^{20} shows an onset of photocurrent at a slightly higher voltage than that for the Nb-STO substrate. This can be explained by presence of surface states in porous STO 10^{20} [68,69]. This phenomenon is discussed in detail in the supplementary information. Porous STO 10^{17} shows negligible photocurrent compared to both porous STO 10^{20} and the Nb-STO substrate, consistent with the lower charge carrier concentration in porous STO 10^{17}.

Figure 3 (d) shows the chronoamperometry results, measured at 0.5 V vs. Ag/AgCl (3M KCl) and under a tungsten halogen lamp at 100 mW/cm^2. As shown in the supplementary information, the spectrum of the lamp has emission mainly in the visible and infra-red region (500 nm – 1000 nm). Interestingly, the porous STO 10^{20} chronoamperometry curves show spikes when the light is turned on before settling to a lower steady state current value. This behaviour further supports the presence of surface states [69–72].

Figure 3(e) shows the Incident Photon to Current Efficiency (IPCE) values for the three samples, measured at an applied bias of 0.3 V vs. Ag/AgCl. As expected for a large bandgap semiconductor like STO (bandgap 3.2 eV), there is very little photocurrent from the visible region of the light spectrum, and all three samples show low IPCE values at higher wavelengths. However, for lower wavelengths corresponding to the UV region, we see that

porous STO 10^{20} shows a much higher IPCE compared to both the Nb-STO substrate and porous STO 10^{17}. As reported in the literature[73,74], the IPCE curves peak at wavelengths between 320 nm and 340 nm. The decrease of the efficiency values for wavelengths smaller than 320 nm in non-passivated samples can be attributed to surface recombination losses[13,73].

Figure 3(f) shows the UV-vis absorption spectra of all the samples. Porous STO 10^{20} shows slightly higher absorption closer to the band-edge of STO. This can be attributed to the presence of oxygen vacancy states below the conduction band, thus permitting more light to be absorbed in the visible range[75–77]. On the other hand, this higher absorption does not translate into higher photocurrent in this range, as can be seen in the IPCE plots (Figure 3(e)). The improvement in the efficiency is in the same wavelength range where it was showing higher efficiency in the Nb-STO substrate. Hence, the oxygen vacancies only contribute towards increasing the charge carrier density and not towards increasing the photocurrent because of more absorption in the visible range. This is corroborated by several other reports[12,33,62].

We now turn to analysis of the flat band potential (V_{fb}) and charge carrier density (N_D) measurements. A high value (more negative) value of V_{fb} is beneficial to aid charge separation and an optimum value of N_D is required for excellent electrical conductivity to transport the separated charge carriers. The charge carrier density N_D and the flat band potential V_{fb} are determined from $1/C^2$ vs. V plots. For the two samples porous STO 10^{17} and Nb-STO substrate, the results were fairly linear (Figure 4(a) and 4(b)) and hence were fitted as per the traditional Mott-Schottky equation[78]:

$$\frac{1}{C^2} = \frac{2}{eA^2\varepsilon_0\varepsilon_r N_D}\left(\left(V - V_{fb}\right) - \frac{\kappa T}{e}\right) \qquad (2)$$

Where C is the capacitance of the semiconductor-electrolyte interface, e is the electronic charge, A is the interfacial area, ε_0 is the permittivity of vacuum, ε_r is relative permittivity of

the semiconductor with respect to vacuum, N_D is the majority charge carrier density in the semiconductor per cubic cm, V is the applied potential, V_{fb} is the flat band potential of the semiconductor electrode in given electrolyte solution, κ is the Boltzmann's constant and T is the temperature. For these plots, V_{fb} is determined from the x-intercept of the linear fits as per the Mott-Schottky relation (eq. 2) and N_D is determined from the slope of these linear fits. In this expression, we excluded the component $\kappa T/e$, because of its low value.

For the porous STO 10^{20} sample, the $1/C^2$ vs. V plots were non-linear and hence were fitted to a quadratic expression (see Figure 4(c)). This expression is given in equation 3 below, and it has been used previously for highly doped samples[79,80].

$$\frac{1}{C^2} = \frac{2}{e\varepsilon_r\varepsilon_o N_D A}\left(V - V_{fb}\right) + \frac{1}{b^2\varepsilon_o^2}\left(V - V_{fb}\right)^2 \qquad (3)$$

Where all the symbols have the same meanings as for equation 2, except for b which is a constant. From the parabolic fit of the data as per the equation above, values for V_{fb} and N_D were approximately determined.

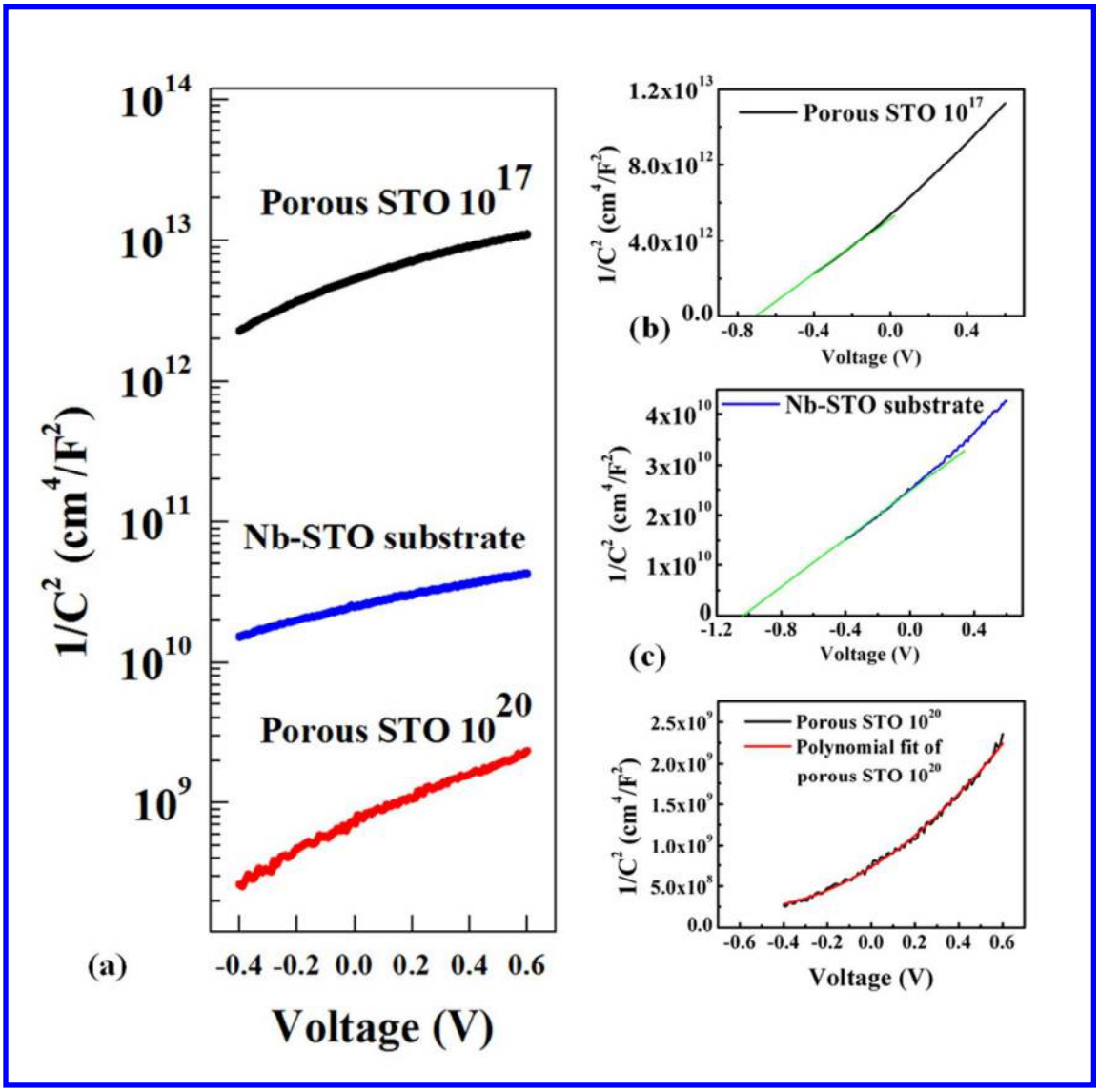

Figure 4: $1/C^2$ vs. V plots of various samples measured at 1 kHz with an amplitude of 10 mV. (a) The results for the three samples studied - porous STO 10^{20}, Nb-STO substrate and porous STO 10^{17} shown together in logarithmic scale, (b) and (c) Mott-Schottky linear fits of the results for porous STO 10^{17} and Nb-doped substrate, respectively and (d) polynomial fit of the results for porous STO 10^{20}.

All the samples showed a positive slope in the $1/C^2$ vs. V plots, thus confirming their n-type behaviour. From Figure 4(a), we can see that the $1/C^2$ values for porous STO 10^{17} are the highest at all biases, whereas those of porous STO 10^{20} are the lowest. This indicates that

the effective capacitance of porous STO 10^{17} is much higher than that of porous STO 10^{20}, consistent with porous STO 10^{17} being much more resistive than porous STO 10^{20}. The charge carrier density N_D is calculated from equation 2 using the slopes of the linear fits of these plots. The x-intercepts of the linear fits give the values of V_{fb}, i.e., the applied bias at which there is no band-bending[78]. The values of V_{fb} and N_D are presented in Table 1.

N_D in porous STO 10^{17} was found to be lower than that of porous STO 10^{20}. Porous STO 10^{20} showed an unexpectedly high flat band potential compared to the other samples. This can be explained by presence of surface states from oxygen vacancy defects pinning the Fermi level[68,81–83]. As discussed in more detail in the supplementary section, electrochemical impedance spectroscopy confirmed the presence of surface states in unpassivated porous STO 10^{20}. It is well known that the photocurrent of oxygen-deficient samples can be improved further by passivating the surface states with suitable chemicals like Al_2O_3[68,70,84]. Thus, perhaps the next step towards improving the PEC performance of these mesoporous samples would be surface passivation by a very thin layer of Al_2O_3.

To conclude, a very simple yet elegant method of growing highly oriented, epitaxial crystalline, very high surface area mesoporous films with tunable electronic properties has been demonstrated. The film shows very high photocatalytic performance. The approach combines the benefits of using physical vapour growth to give very high quality, reusable material with the benefits of having a very high surface area, which is normally only achieved using chemical growth. Substrate-supported mesoporous structures are achieved by first growing epitaxial columnar nanocomposite films, followed by selective etching out of one phase. By carrier concentration tuning via doping, the oriented, mesoporous STO thin films give very high efficiencies.

Experimental Section:

Fabrication: The columnar composite thin films of STO-MgO were deposited by laser ablation of a composite target containing STO and MgO. The targets were made by mixing and grinding STO and MgO nanopowders in equal weight proportion, followed by uniaxial pressing under 100kN for 10 minutes to form the pellets. The pellets were then sintered in oxygen flow rate of 40 sccm to 1100 °C for 6 hours. The laser energy used for the pulsed laser deposition of the thin films was ~ 2 J/cm^2 and the laser pulse frequency was 1Hz. The Nb-STO substrates were heated to 770-800 °C, in an oxygen flow rate of 9.8 sccm with 0.2 mbar pressure inside the deposition chamber. The deposition rate was 10 nm/min. After the deposition, the films were annealed at 650 °C in situ at 400 mbar and 0.2 mbar of O_2 pressure for one hour, respectively, for porous STO 10^{17} and porous STO 10^{20}. To achieve a mesoporous STO film, the MgO phase was selectively etched out from the films by dipping them in 20% acetic acid solution at 60 °C for 30 minutes.

Characterisation: A four circle diffractometer was used for X-ray diffraction. A scanning electron microscope (SEM) was used to capture the surface images. The surface area of the mesoporous films was calculated using image analysis software to determine the average pore circumference from the plan-view SEM images. To compute the surface area of the pores, the values were multiplied by the number of pores, and the pore-length, which is equivalent to the film thickness. (Note: The area used for calculating photocurrent and IPCE data was the projected (plan-view) surface area under illumination for the sample, whereas for the $1/C^2$ vs. V plots, the area used was the estimated curved surface area of the nanowalls or cavities formed after etching out the nanocolumns. For simplicity, the area of the sample forming the 'cross-sections' of the nanowalls was ignored on account of being very small.). A photoelectrochemical work station coupled with a tungsten halogen lamp (Zahner WOW01) was used for photoelectrochemical characterisation. The lamp had very little UV component.

A comparison of the lamp's spectrum with the AM1.5 G is presented in the supplementary information. The electrolyte used for the photoelectrochemical measurements was 0.5 M NaOH solution. An in-house made photoelectrochemical cell with quartz windows and polytetrafluoroethylene (PTFE) walls was used. A Pt wire as a counter electrode and an Ag/AgCl (3M KCl) reference electrode were used for these measurements. The DC bias was varied from -0.8 V to 1.8 V Ag/AgCl (3M KCl) for the J-V curves in both dark and light conditions. The $1/C^2$ vs. V measurements were carried out from -0.4 V to 0.8 V vs. Ag/AgCl (3M KCl) with an AC disturbance of 10 mV at 1 kHz. Electrochemical impedance spectroscopy (EIS) measurements were performed for the frequency range 0.1 Hz to 1 kHz and at 0V vs. Ag/AgCl (3M KCl) reference electdrode. The EIS data was fitted using ZView software suit. The IPCE data was recorded using a quantum efficiency measurement system at 0.3 V vs. Ag/AgCl (3M KCl) electrode and in 0.5 M NaOH solution. A UV-VIS-NIR spectrophotometer was for acquiring UV-Vis spectra from 200 nm to 800 nm. The films for optical characterisation were grown on $LaAlO_3$ (001) single crystal substrates under the same deposition conditions as used for the films grown on Nb-STO. The films used for UV-vis spectroscopy were grown on $LaAlO_3$ because of its similar structure as that of Nb-STO, which is essential for the heteroepitaxial growth of the two phases and because of the large bandgap (5.2 eV) of $LaAlO_3$, thus allowing to detect any blue or red shifts in the band-edges of these thin films.

Acknowledgements: We gratefully acknowledge the support from the Cambridge Commonwealth Trust, ERC adg grant (247276) NOVOX and UKIERI grant (IND/CONT/E/12-13/813). The TEM work at Texas A&M University is funded by the US National Science Foundation (DMR-1401266). We also acknowledge the help from Y. J. Liu and V. Kumar for the preliminary measurements for this project. We thank Dr. Oon Jew Lee for her help during initial etching set up. We thank Mary Vickers for her help with the X-ray

diffraction. We thank Dr. Reza Saberi Moghaddam for his help with passivation related matters. We thank Professor A. K. Cheetham for use of the UV-vis spectrophotometer in his lab.

Associated Content: Supporting Information file. Plots of Electrochemical Impedance Spectroscopy data, discussion of charge transfer mediated through surface states and band bending, and emission spectrum of the lamp compared with the AM 1.5G spectrum.

References:

(1) Fujishima, A.; Honda, K. *Nature* **1972**, *238* (5358), 37–38.

(2) Woodhouse, M.; Parkinson, B. A. *Chem. Soc. Rev.* **2009**, *38* (1), 197–210.

(3) Chandrasekaran, S.; McInnes, S. J. P.; Macdonald, T. J.; Nann, T.; Voelcker, N. H. *RSC Adv.* **2015**, *5* (104), 85978–85982.

(4) Ashcheulov, P.; Kusko, M.; Fendrych, F.; Poruba, A.; Taylor, A.; Jager, A.; Fekete, L.; Kraus, I.; Kratochvilova, I. *Phys. Status Solidi A* **2014**, No. 10, 2347–2352.

(5) Warren, E. L.; Boettcher, S. W.; McKone, J. R.; Lewis, N. S. **2010**, *7770*, 77701F–77701F–7.

(6) Price, M. J.; Maldonado, S. *J. Phys. Chem. C* **2009**, *113* (Figure 1), 11988–11994.

(7) Hu, S.; Shaner, M. R.; Beardslee, J. A.; Lichterman, M.; Brunschwig, B. S.; Lewis, N. S. *Science* **2014**, *344* (6187), 1005–1009.

(8) Rajeshwar, K. *J. Appl. Electrochem.* **2007**, *37* (7), 765–787.

(9) Hu, J.; Zhu, F.; Matulionis, I.; Gaillard, N.; Deutsch, T.; Wang, H. In *White Papers on Materials for Photoelectrochemical Water Splitting*; 2013.

(10) Prevot, M.; Sivula, K. *J. Phys. Chem. C* **2013**, *117* (17879–17893).

(11) Rajeshwar, K. In *Encyclopedia of Electrochemistry*; 2007.

(12) Wrighton, M. S.; Ellis, A. B.; Wolczanski, P. T.; Morse, D. L.; Abrahamson, H. B.; Ginley, D. S. *J. Am. Chem. Soc.* **1976**, *98* (10), 2774–2779.

(13) Tomkiewicz, M.; Fay, H. *Appl. Phys.* **1979**, *18* (1), 1–28.

(14) Maruska, H. P.; Ghosh, A. K. *Sol. Energy Mater.* **1979**, *1* (3–4), 237–247.

(15) Tonda, S.; Kumar, S.; Anjaneyulu, O.; Shanker, V. *Phys. Chem. Chem. Phys.* **2014**, *16* (43), 23819–23828.

(16) Wang, D.; Ye, J.; Kako, T.; Kimura, T. *J. Phys. Chem. B* **2006**, *110* (32), 15824–15830.

(17) Wei, W.; Dai, Y.; Guo, M.; Yu, L.; Huang, B. *J. Phys. Chem. C* **2009**, *113*, 15046–15050.

(18) Wang, J.; Li, H.; Li, H.; Yin, S.; Sato, T. *Solid State Sci.* **2009**, *11* (1), 182–188.

(19) Guo, K.; Liu, Z.; Wang, Y.; Zhao, Y.; Xiao, Y.; Han, J.; Li, Y.; Wang, B.; Cui, T. *Int. J. Hydrogen Energy* **2014**, *39* (25), 13408–13414.

(20) Zhang, J.; Bang, J. H.; Tang, C.; Kamat, P. V. *ACS Nano* **2010**, *4* (1), 387–395.

(21) Mavroides, J. G.; Kafalas, J. A.; Kolesar, D. F. *Appl. Phys. Lett.* **1976**, *28* (5), 241–243.

(22) Pinheiro, A. N.; Firmiano, E. G. S.; Rabelo, A. C.; Dalmaschio, C. J.; Leite, E. R. *RSC Adv.* **2014**, *4* (4), 2029–2036.

(23) Wrighton, M. S. *Acc. Chem. Res.* **1979**, *12* (9), 303–310.

(24) Bera, A.; Wu, K.; Sheikh, A.; Alarousu, E.; Mohammed, O. F.; Wu, T. *J. Phys. Chem. C* **2014**, *118* (49), 28494–28501.

(25) Liu, M.; Nam, C.-Y.; Black, C. T.; Kamcev, J.; Zhang, L. *J. Phys. Chem. C* **2013**, *117* (26), 13396–13402.

(26) Iwashina, K.; Kudo, A. *J. Am. Chem. Soc.* **2011**, *133* (34), 13272–13275.

(27) Asai, R.; Nemoto, H.; Jia, Q.; Saito, K.; Iwase, A.; Kudo, A. *Chem. Commun.* **2014**, *50* (19), 2543–2546.

(28) Shen, P.; Lofaro, J. C. J.; Woerner, W. R.; White, M. G.; Su, D.; Orlov, A. *Chem. Eng. J.* **2013**, *223*, 200–208.

(29) Niishiro, R.; Tanaka, S.; Kudo, A. *Appl. Catal. B Environ.* **2014**, *150–151*, 187–196.

(30) Liu, Y.; Xie, L.; Li, Y.; Yang, R.; Qu, J.; Li, Y.; Li, X. *J. Power Sources* **2008**, *183* (2), 701–707.

(31) Paramasivam, I.; Jha, H.; Liu, N.; Schmuki, P. *Small* **2012**, *8* (20), 3073–3103.

(32) Zhang, X.; Huo, K.; Hu, L.; Wu, Z.; Chu, P. K. *J. Am. Ceram. Soc.* **2010**, *93* (9), 2771–2778.

(33) Wang, G.; Ling, Y.; Li, Y. *Nanoscale* **2012**, *4* (21), 6682.

(34) van de Krol, R.; Liang, Y.; Schoonman, J. *J. Mater. Chem.* **2008**, *18* (20), 2311.

(35) Puangpetch, T.; Sommakettarin, P.; Chavadej, S.; Sreethawong, T. *Int. J. Hydrogen Energy* **2010**, *35* (22), 12428–12442.

(36) Puangpetch, T.; Sreethawong, T.; Yoshikawa, S.; Chavadej, S. *J. Mol. Catal. A Chem.* **2009**, *312* (1–2), 97–106.

(37) Puangpetch, T.; Chavadej, S.; Sreethawong, T. *Energy Convers. Manag.* **2011**, *52* (5), 2256–2261.

(38) Baker, D. R.; Kamat, P. V. *Adv. Funct. Mater.* **2009**, *19* (5), 805–811.

(39) Innocenzi, P.; Malfatti, L. *Chem. Soc. Rev.* **2013**, *42* (9), 4198–4216.

(40) Bruce, P. G.; Scrosati, B.; Tarascon, J.-M. *Angew. Chem. Int. Ed. Engl.* **2008**, *47* (16), 2930–2946.

(41) Lee, U.; Min-Hye, K.; Young-Uk, K. *Bull. Korean Chem. Soc.* **2006**, *27* (6), 808–816.

(42) Schüth, F. *Chem. Mater.* **2001**, *13*, 3184–3195.

(43) Crepaldi, E. L.; Soler-Illia, G. J. D. A. A.; Grosso, D.; Cagnol, F.; Ribot, F.; Sanchez, C. *J. Am. Chem. Soc.* **2003**, *125*, 9770–9786.

(44) Amani Hamedani, H.; Khaleel, J. A.; Dahmen, K.-H.; Garmestani, H. *Cryst. Growth Des.* **2014**, *14* (10), 4911–4919.

(45) Xin, Y.; Jiang, J.; Huo, K.; Hu, T.; Chu, P. K. *ACS Nano* **2009**, *3* (10), 3228–3234.

(46) Liu, J.; Sun, Y.; Li, Z.; Li, S.; Zhao, J. *Int. J. Hydrogen Energy* **2011**, *36* (10), 5811–5816.

(47) Yang, Y.; Lee, K.; Kado, Y.; Schmuki, P. *Electrochem. commun.* **2012**, *17*, 56–59.

(48) Jiao, Z.; Chen, T.; Yu, H.; Wang, T.; Lu, G.; Bi, Y. *J. Colloid Interface Sci.* **2014**, *419*, 95–101.

(49) Wu, Z.; Su, Y.; Yu, J.; Xiao, W.; Sun, L.; Lin, C. *Int. J. Hydrogen Energy* **2015**, *40* (31), 9704–9712.

(50) Wang, F.; Liu, Y.; Ma, Z.; Li, H.; Kang, Z.; Shen, M. *New J. Chem.* **2013**, *37* (2), 290.

(51) Hertkorn, D.; Elsenheimer, H. C.; Bruch, R.; Paul, F.; Müller, C.; Hanemann, T.; Reinecke, H. *J. Appl. Phys.* **2013**, *114* (2), 27020.

(52) Zhao, L.; Fang, L.; Dong, W.; Zheng, F.; Shen, M.; Wu, T. *Appl. Phys. Lett.* **2013**, *102* (12), 121905.

(53) Katayama, M.; Ishihara, T.; Matsumoto, Y.; Kubota, J.; Domen, K. In *218th Electrochemical Society Meeting*; 2010.

(54) Willmott, P. R.; Huber, J. R. *Rev. Mod. Phys.* **2000**, *72* (1), 315–328.

(55) Djurišić, A. B.; Tam, K. H.; Cheung, C. K.; Leung, Y. H.; Ling, C. C.; Beling, C. D.; Fung, S.; Chan, W. K. In *Nanoscale Phenomena: Basic Science to Device Applications*; Springer Science & Business Media, 2007; pp 117–130.

(56) Jiao, Z.; Chen, T.; Xiong, J.; Wang, T.; Lu, G.; Ye, J.; Bi, Y. *Sci. Rep.* **2013**, *3*, 2720.

(57) Das, R.; Kumar, A.; Kumar, Y.; Sen, S.; Shirage, P. M. *RSC Adv.* **2015**, *5* (74), 60365–60372.

(58) Zhang, W.; Chen, A.; Bi, Z.; Jia, Q.; Macmanus-Driscoll, J. L.; Wang, H. *Curr. Opin. Solid State Mater. Sci.* **2014**, *18* (1), 6–18.

(59) Sun, Y.; Liu, J.; Li, Z. *J. Solid State Chem.* **2011**, *184* (8), 1924–1930.

(60) Krebs, H.; Weisheit, M.; Erik, S.; Scharf, T.; Fuhse, C.; St, M.; Sturm, K.; Seibt, M.; Kijewski, H.; Nelke, D.; Panchenko, E.; Buback, M. *Adv. Solid State Phys.* **2003**, *43*, 505–518.

(61) Jin, K. X.; Li, Y. F.; Wang, Z. L.; Peng, H. Y.; Lin, W. N.; Kyaw, a. K. K.; Jin, Y. L.; Jin, K. J.; Sun, X. W.; Soci, C.; Wu, T. *AIP Adv.* **2012**, *2* (4), 0–9.

(62) Tan, H.; Zhao, Z.; Zhu, W.; Coker, E. N.; Li, B.; Zheng, M.; Yu, W.; Fan, H.; Sun, Z. *ACS Appl. Mater. Interfaces* **2014**, *6* (21), 19184–19190.

(63) Liu, M.; Lyons, J. L.; Yan, D.; Hybertsen, M. S. *Adv. Funct. Mater.* **2015**, n/a-n/a.

(64) Fu, Z.; Jiang, T.; Liu, Z.; Wang, D.; Wang, L.; Xie, T. *Electrochim. Acta* **2014**, *129*, 358–363.

(65) Wang, C.; Chen, Z.; Jin, H.-B.; Cao, C.; Li, J.; Mi, Z. *J. Mater. Chem. A* **2014**.

(66) Tamura, H.; Yoneyama, H.; Iwakura, C.; Sakamoto, H.; Murakami, S. *J. Electroanal. Chem. Interfacial Electrochem.* **1977**, *80*, 357–363.

(67) Kawasaki, S.; Takahashi, R.; Akagi, K.; Yoshinobu, J.; Komori, F.; Horiba, K.; Kumigashira, H.; Iwashina, K.; Kudo, A.; Lippmaa, M. *J. Phys. Chem. C* **2014**, *118*, 20222–20228.

(68) Liu, R.; Zheng, Z.; Spurgeon, J.; Yang, X. *Energy Environ. Sci.* **2014**, 2504–2517.

(69) Le Formal, F.; Tétreault, N.; Cornuz, M.; Moehl, T.; Grätzel, M.; Sivula, K. *Chem. Sci.* **2011**, *2* (4), 737.

(70) Le Formal, F.; Sivula, K.; Grätzel, M. *J. Phys. Chem. C* **2012**, *116* (51), 26707–26720.

(71) Peter, L. M.; Li, J.; Peat, R. *J. Electroanal. Chem.* **1984**, *165* (1–2), 29–40.

(72) Wolcott, A.; Smith, W. a; Kuykendall, T. R.; Zhao, Y.; Zhang, J. Z. *Small* **2009**, *5* (1), 104–111.

(73) Mavroides, J. G.; Kafalas, J. a.; Kolesar, D. F. *Appl. Phys. Lett.* **1976**, *28* (5), 241–243.

(74) Rajeshwar, K.; Singh, P.; DuBow, J. *Electrochim. Acta* **1978**, *23* (11), 1117–1144.

(75) Yin, J.; Ye, J.; Zou, Z. *Appl. Phys. Lett.* **2004**, *85* (4), 689–691.

(76) Kumar, A.; Dho, J. *Curr. Appl. Phys.* **2013**, *13* (4), 768–774.

(77) Mochizuki, S.; Fujishiro, F.; Ishiwata, K.; Shibata, K. *Phys. B Condens. Matter* **2006**, *376–377* (1), 816–819.

(78) Gelderman, K.; Lee, L.; Donne, S. W. *J. Chem. Educ.* **2007**, *84* (4), 685.

(79) Suzuki, S.; Yamamoto, T.; Suzuki, H.; Kawaguchi, K.; Takahashi, K.; Yoshisato, Y. *J. Appl. Phys.* **1997**, *81* (10), 6830.

(80) Matsumoto, Y.; Takata, S.; Tanaka, R.; Hachiya, A. *J. Appl. Phys.* **2011**, *109* (1), 14112.

(81) Nagasubramanian, G.; Wheeler, B. L.; Fan, F.-R. F.; Bard, A. J. *J. Electrochem. Soc.* **1982**, *129* (10), 2224.

(82) Abruña, H. D. *J. Electrochem. Soc.* **1982**, *129* (10), 2224.

(83) Pyper, K. J.; Yourey, J. E.; Bartlett, B. M. *J. Phys. Chem. C* **2013**, *117*, 24726–24732.

(84) Hwang, Y. J.; Hahn, C.; Liu, B.; Yang, P. *ACS Nano* **2012**, *6* (6), 5060–5069.

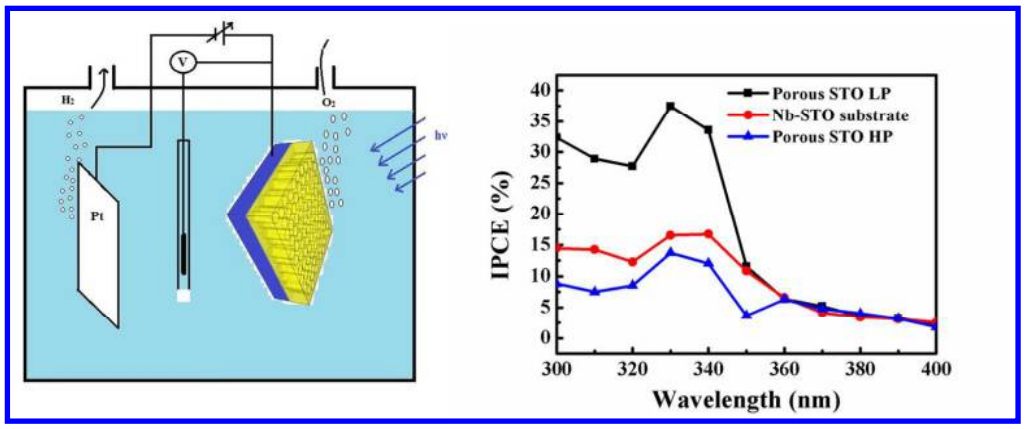

Very high surface area mesoporous thin films grown by pulsed laser deposition (PLD) for photoelectrochemical water splitting
Very high surface area mesopor
411x166mm (96 x 96 DPI)